NSRRC-J043794 (2014)

Nanoscale

PAPER

View Article Online
View Journal | View Issue

Published on 29 January 2014. Downloaded by National Tsing Hua University on 07/07/2014 02:07:48.

Cite this: *Nanoscale*, 2014, 6, 5208

Co-crystallization phase transformations in all π-conjugated block copolymers with different main-chain moieties†

Yi-Huan Lee,[ab] Wei-Chih Chen,[b] Yi-Lung Yang,[b] Chi-Ju Chiang,[a] Tsutomu Yokozawa[c] and Chi-An Dai*[ab]

Received 13th November 2013
Accepted 24th January 2014

DOI: 10.1039/c3nr06037c

www.rsc.org/nanoscale

Driven by molecular affinity and balance in the crystallization kinetics, the ability to co-crystallize dissimilar yet self-crystallizable blocks of a block copolymer (BCP) into a uniform domain may strongly affect its phase diagram. In this study, we synthesize a new series of crystalline and monodisperse all-π-conjugated poly(2,5-dihexyloxy-*p*-phenylene)-*b*-poly(3-(2-ethylhexyl)thiophene) (PPP–P3EHT) BCPs and investigate this multi-crystallization effect. Despite vastly different side-chain and main-chain structures, PPP and P3EHT blocks are able to co-crystallize into a single uniform domain comprising PPP and P3EHT main-chains with mutually interdigitated side-chains spaced in-between. With increasing P3EHT fraction, PPP–P3EHTs undergo sequential phase transitions and form hierarchical superstructures including predominately PPP nanofibrils, co-crystalline nanofibrils, a bilayer co-crystalline/pure P3EHT lamellar structure, a microphase-separated bilayer PPP–P3EHT lamellar structure, and finally P3EHT nanofibrils. In particular, the presence of the new co-crystalline lamellar structure is the manifestation of the interaction balance between self-crystallization and co-crystallization of the dissimilar polymers on the resulting nanostructure of the BCP. The current study demonstrates the co-crystallization nature of all-conjugated BCPs with different main-chain moieties and may provide new guidelines for the organization of π-conjugated BCPs for future optoelectronic applications.

1. Introduction

During the past decades, π-conjugated polymers have attracted great attention because they possess unique optoelectronic properties for uses in low-cost, large-area, and flexible optoelectronic devices including organic photovoltaic cells,[1,2] light-emitting diodes,[3] and thin-film transistors.[4,5] It has been widely accepted that the performance of these fabricated devices is critically dependent on the molecular packing of the π-conjugated polymers.[6–8] Therefore, controlling the organization feature and crystalline morphology of these semiconducting polymer materials is being pursued as a means to optimize the device performance.[9,10]

The use of rod–coil block copolymers (BCPs), wherein a π-conjugated polymer is covalently connected to another insulating block, offers an attractive strategy to precisely control the orientation and nanostructures in conjugated polymers since these materials can spontaneously self-organize into well-defined microphase separated domains with nanoscale dimensions.[11–19] This approach offered a facile route towards the fabrication of organic solar cells with a desired nanostructure and domain size in a range comparable to the exciton diffusion length, maximized interfacial area for charge separation, and enhanced stability for extended device operation.[20,21] However, despite the structural advantages of these materials, it is generally believed that the insulating block of the rod–coil BCPs may strongly deteriorate the optoelectronic properties in their devices, thereby degrading the device performance. For the purpose of overcoming these drawbacks, the development of BCPs comprising all π-conjugated rod–rod blocks instead of a rod–coil one is currently becoming an emerging field. A number of experimental studies on the phase behavior of the all-conjugated BCPs have been developed.[22–38] These studies demonstrate that combining two dissimilar π-conjugated blocks within BCPs will allow for a controlled spatial arrangement of these blocks in complex ordered nanostructures.

Recently, Qiu *et al.* pointed out that poly(3-butylthiophene)-*b*-poly(3-hexylthiophene) BCPs have the ability of co-crystallizing into a uniform crystal domain, which may strongly affect their optoelectronic properties.[39] Additionally, Su *et al.* also reported the co-crystalline structure of the poly(3-

[a]*Department of Chemical Engineering and Institute of Polymer Science and Engineering, National Taiwan University, No. 1 Roosevelt Rd Sec. 4, Taipei 10617, Taiwan. E-mail: polymer@ntu.edu.tw*

[b]*Institute of Polymer Science and Engineering, National Taiwan University, Taipei 10617, Taiwan*

[c]*Department of Material & Life Chemistry, Kanagawa University, Rokkakubashi Kanagama-ku, Yokohama 221-8686, Japan*

† Electronic supplementary information (ESI) available: Detailed synthesis procedures, and XRD and TEM characterization data of polymer samples. See DOI: 10.1039/c3nr06037c

This journal is © The Royal Society of Chemistry 2014

Published on 29 January 2014. Downloaded by National Tsing Hua University on 07/07/2014 02:07:48.

hexylthiophene)-*b*-poly(3-thiophene hexylacetate) system.[40] For these systems, their designing merit is to incorporate poly(3-alkylthiophene) (P3ATs) with different alkyl side-chain lengths/architectures to balance the molecular organization and the phase separation of these materials. However, it should be noted that most of the studies were primarily focused on the all-conjugated copolythiophene block copolymer systems.

So far a systematic study on the co-crystallization structure and the phase transformations of the all-conjugated BCPs with different main-chain moieties has yet to be found possibly due to strong immiscibility or large differences in crystallographic kinetics between the two π-conjugated polymers. However, these systems may provide beneficial optoelectronic properties and be used as a unique platform to study the crystallization, melting behavior and the chain properties of dissimilar π-conjugated polymers due to their novel co-crystallization behavior.

Herein, we reported on the synthesis and self-assembly behavior of a new series of crystalline–crystalline poly(2,5-dihexyloxy-*p*-phenylene)-*b*-poly(3-(2-ethylhexyl)thiophene) (PPP–P3EHT) BCPs. Notably, P3EHT with a branched side-chain which bears higher steric hindrance was so chosen since its self-crystallization is significantly suppressed, compared with that of the mostly used P3AT in the literature, namely P3HT, in which case strong inter-chain π–π interaction between P3HTs may exclude co-crystallization with other dissimilar π-conjugated polymers. The comparable crystallization kinetics and similar repeated monomer unit size of the PPP and P3EHT constituent polymers are the key factors for the formation of cocrystals. PPP–P3EHTs with varying block ratios were found to undergo sequential phase transitions and self-assemble into different hierarchical superstructures. These results demonstrate the competing effects of self-crystallization and co-crystallization on the self-assembling hierarchical superstructure of all-conjugated BCPs with different main-chain moieties and may provide new insights into the self-organization of dissimilar π-conjugated BCPs.

2. Experimental section

Materials

1,4-Dibromo-2,5-dihexyloxybenzene (**4, M1**)[41] and 2-bromo-3-(2-ethylhexyl)-5-iodothiophene (**8, M2**)[22] monomers were synthesized according to the reported procedures from the literature as shown in Scheme S1.† Ultrahigh purity nitrogen was purchased (99.999% pure) and further purified by passing it through a column of molecular sieves and a BTS (Fluka) catalytic oxygen trap. Tetrahydrofuran (THF, Acros, 99.9%) was dried with sodium metal (Sigma-Aldrich, 99%) and benzophenol (Acros, 99%) was used as the indicator for dryness. [1,3-Bis(diphenylphosphino)ethane]dichloronickel(II) (Ni(dppe)Cl_2, Acros, 99%) and isopropylmagnesium (i-PrMgCl, Acros, 2.0 M solution in THF) were used as received without purification.

Synthesis procedure of the PPP–P3EHT block copolymer

All polymerization were prepared by Grignard metathesis (GRIM) polymerization, and the synthetic route for PPP–P3EHT block copolymers is outlined in Scheme 1. In a typical synthesis procedure of PPP–P3EHT block copolymers (*e.g.* **P30E44**, feed molar ratio of 33 : 67), two round-bottom flasks (250 mL) equipped with a three-way stopcock were dried under vacuum and heated followed by cooling them to room temperature. One of the three-neck round bottom flasks was flushed with N_2 and charged with purified 1,4-dibromo-2,5-dihexyloxybenzene (**M1**, 3.0 mmol, 1.31 g) and anhydrous THF (30 mL). After stirring them to uniformity, i-PrMgCl (3.0 mmol, 1.5 mL) was added *via* syringe and the resulting mixture was allowed to stir for another 2 h at a gentle reflux (~70 °C) (solution A). Then, in the other flask, freshly distilled 2-bromo-3-(2-ethylhexyl)-5-iodothiophene (**M2**, 6.0 mmol, 2.41 g) was reacted with i-PrMgCl (6.0 mmol, 3.0 mL) in anhydrous THF (60 mL) at 0 °C for 30 min (solution B). Meanwhile, solution A was cooled down to room temperature

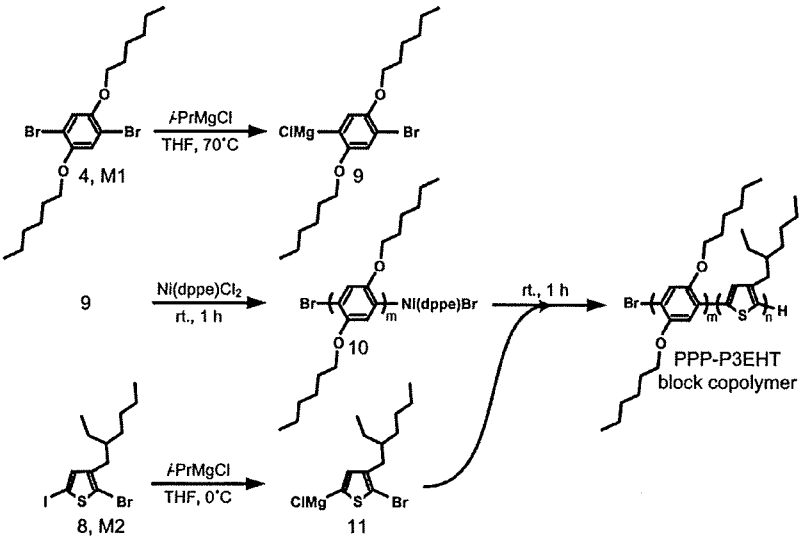

Scheme 1 Synthetic route of PPP–P3EHT block copolymers.

Published on 29 January 2014. Downloaded by National Tsing Hua University on 07/07/2014 02:07:48.

and the Ni(dppe)Cl_2 catalyst (0.27 mmol, 0.14 g) was added through a funnel to the polymerization flask as quickly as possible to ensure all initiations to start at the same time. After stirring for 1 h to obtain the PPP living polymer, an aliquot of the PPP homopolymer was collected and terminated with dry methanol to measure its molecular weight and polydispersity. Then, the GRIM product of **M2** monomers (solution B) was transferred into solution A *via* a stainless needle tube, and the resulting solution was allowed to proceed for copolymerization for 1 h. The reaction was quenched by pouring 5 M hydrochloric acid into the solution and precipitated in methanol followed by Soxhlet extraction in sequence with solvents of methanol, hexane, and chloroform. Finally, the residual chloroform from the polymer was removed by drying in a vacuum oven at room temperature. The final product was dark/red powders and recovered in quantitative yield. The polymers were stored under an inert atmosphere.

P28E109. ^{1}H NMR (400 MHz, $CDCl_3$, ppm): δ 7.06 (s, 2.00H, Ar-*H*), 6.91 (s, 4.56H, Ar-*H*), 3.88 (br, 4.00H, Ar-OCH_2), 2.70 (br, 9.11H, Ar-CH_2–), 1.68 (m, 8.55H), 1.34–1.27 (m, 48.4H, –CH_2–), 0.86 (br, 33.3H, –CH_3). M_w: 14.9k and PDI: 1.09.

P32E64. ^{1}H NMR (400 MHz, $CDCl_3$, ppm): δ 7.06 (s, 2.00H, Ar-*H*), 6.91 (s, 2.80H, Ar-*H*), 3.89 (br, 4.00H, Ar-OCH_2), 2.70 (br, 5.60H, Ar-CH_2–), 1.68 (br, 6.80H), 1.34–1.27 (m, 34.4H, –CH_2–), 0.86 (br, 22.8H, –CH_3). M_w: 10.8k and PDI: 1.10.

P32E53. ^{1}H NMR (400 MHz, $CDCl_3$, ppm): δ 7.06 (s, 2.00H, Ar-*H*), 6.91 (s, 2.51H, Ar-*H*), 3.88 (br, 4.00H, Ar-OCH_2), 2.70 (br, 5.02H, Ar-CH_2–), 1.67 (br, 6.51H), 1.34–1.26 (m, 32.1H, –CH_2–), 0.86 (br, 21.1H, –CH_3). M_w: 10.0k and PDI: 1.16.

P30E44. ^{1}H NMR (400 MHz, $CDCl_3$, ppm): δ 7.06 (s, 2.00H, Ar-*H*), 6.91 (s, 2.02H, Ar-*H*), 3.89 (br, 4.00H, Ar-OCH_2–), 2.70 (br, 4.04H, Ar-CH_2–), 1.66 (br, 6.02H), 1.32–1.27 (m, 28.2H, –CH_2–), 0.86 (br, 18.1H, –CH_3). M_w: 8.7k and PDI: 1.16.

P29E28. ^{1}H NMR (400 MHz, $CDCl_3$, ppm): δ 7.06 (s, 2.00H, Ar-*H*), 6.91 (s, 1.21H, Ar-*H*), 3.89 (br, 4.00H, Ar-OCH_2–), 2.70 (br, 2.41H, Ar-CH_2–), 1.65 (br, 5.21H), 1.31–1.25 (m, 21.7H, –CH_2–), 0.86 (br, 13.3H, –CH_3). M_w: 6.6k and PDI: 1.13.

P33E15. ^{1}H NMR (400 MHz, $CDCl_3$, ppm): δ 7.06 (s, 2.00H, Ar-*H*), 6.91 (s, 0.65H, Ar-*H*), 3.89 (br, 4.00H, Ar-OCH_2–), 2.70 (br, 1.29H, Ar-CH_2–), 1.65 (br, 4.65H), 1.32–1.25 (m, 17.2H, –CH_2–), 0.84 (br, 9.88H, –CH_3). M_w: 5.3k and PDI: 1.10.

P33E6. ^{1}H NMR (400 MHz, $CDCl_3$, ppm): δ 7.06 (s, 2.00H, Ar-*H*), 6.91 (s, 0.32H, Ar-*H*), 3.89 (br, 4.00H, Ar-OCH_2–), 2.70 (br, 0.65H, Ar-CH_2–), 1.64 (br, 4.32H), 1.31–1.24 (m, 14.6H, –CH_2–), 0.84 (br, 7.95H, –CH_3). M_w: 4.7k and PDI: 1.17.

Characterization methods

The molecular weight and molecular weight distribution of the synthesized block copolymers were measured by using a GPC (Waters 2695) equipped with two Styragel columns (HR3 and HR4E), a refractive index detector (Waters 2414) and a photodiode array absorbance detector (Waters 2996). THF was used as the mobile phase at a flow rate of 1 mL min^{-1} and monodispersed polystyrene standards (Pressure Chemicals) were used for the system calibration. The synthesized block copolymers were dissolved in $CDCl_3$ and their ^{1}H-NMR spectra were recorded using a 400 MHz Bruker Avance spectrometer at room temperature. NMR spectra were reported in ppm. Splitting patterns were designated as s (singlet), m (multiplet), and br (broad resonance). SAXS and WAXS experiments were performed separately on the beamline 23A1 and 13A1 at the National Synchrotron Radiation Research Center (NSRRC) in Taiwan. All tested samples were prepared *via* a slow drying method from their THF solution (10 mg mL^{-1}) in a washer, sealed between two thin Kapton® windows, heat-treated above the melting temperature of the copolymers and then annealed at 40 °C for 1 day. All TEM samples for the bulk equilibrium morphology measurements were prepared *via* the same preparation method as the SAXS and WAXS samples. The bulk samples were cut into thin films using a Reichert Ultracut microtome with a diamond knife. Ultrathin sections of TEM samples (thickness < 100 nm) were then stained with RuO_4 vapors for P3EHT domains as a function of exposure time from 3 min to 30 min (Fig. S3†). The best result was found for 5 min of RuO_4 exposure. TEM imaging was performed using a JEOL 1230 microscope operating at 120 kV with a Gatan CCD camera in the bright field mode. Thermal analysis was performed using a Perkin-Elmer Diamond differential scanning calorimeter equipped with an intracooler. All samples were prepared *via* a slow drying method from their THF solution and then sealed in aluminum pans for the analysis. The samples were annealed at 40 °C for 1 day prior to DSC analysis and then operated at a heating rate of 10 °C min^{-1} and a cooling rate of 10 °C min^{-1} from 110 to 0 °C under N_2. The surface morphology of PPP–P3EHT films was also characterized by using atomic force microscopy. Tapping mode images were acquired by using a Seiko E-sweep SPM equipped with a SII NanoNavi probe station. A polygon based pyramid-shaped silicon tip was applied in dynamic force mode (DFM) experiments using a type of SI-DF20 with a spring force constant of 16 N m^{-1} and a resonance frequency of 135 kHz. The scan rate was set at 1 Hz. The films were spin-coated from 10 mg mL^{-1} block copolymer solution in THF on a silicon wafer, followed by annealing them at 40 °C for 1 day.

3. Results and discussion

The Grignard metathesis (GRIM) polymerization has been reported by McCullough and Yokozawa *et al.* to offer the control over several major molecular properties of the copolymers, such as molecular weight and polydispersity.[41–44] A living PPP block was first obtained from 1-bromo-4-chloromagnesio-2,5-dihexyloxybenzene monomers with a Ni catalyst, followed by the addition of 2-bromo-5-chloromagnesio-3EHT monomers to yield the BCPs.[23,27,45,46] Before polymerization with the GRIM product of **M2** monomers, the molecular weight of the PPP homopolymer was measured by gel permeation chromatography (GPC) to confirm the molecular weight characterization (M_n = 3.0k), and the polydispersity index (PDI) of all PPP samples was less than 1.1. Finally, all obtained block copolymers were characterized by GPC (Fig. 1) to show a monomodal molar mass distribution with an overall polydispersity (M_w/M_n) less than 1.2. The BCPs with a fixed PPP M_n of around 3000 g per

 This journal is © The Royal Society of Chemistry 2014

Published on 29 January 2014. Downloaded by National Tsing Hua University on 07/07/2014 02:07:48.

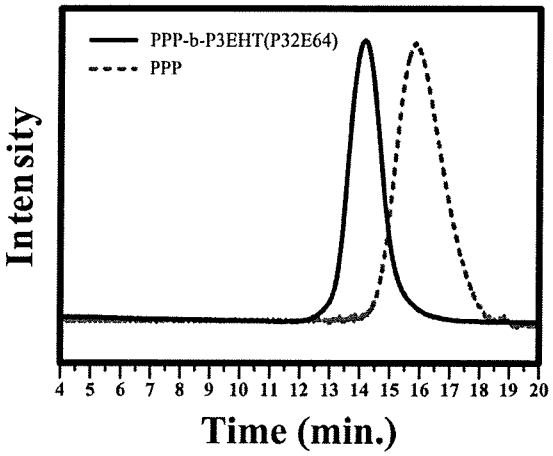

Fig. 1 GPC chart of the PPP–P3EHT (**P32E64**) diblock copolymer (black line) and the PPP precursor (red dash line) prior to adding the monomers of P3EHT.

mole and varied P3EHT M_n (from 600 to around 10 000 g per mole) were denoted as PXXEYY, where P and E stand for PPP and P3EHT segments, respectively, while XX and YY represent their molecular weight (in the unit of 100 g mol^{-1}) as summarized in Table 1. For example, based on the ^{1}H NMR spectrum shown in Fig. 2, the mole fraction of P3EHT in the **P30E44** block copolymer was estimated to be ~67% which was calculated by the integrated area ratio between the aromatic $-CH_2-$ signal (δ = 2.70 ppm) of the alkoxy side-chain of P3EHT and the aromatic $-OCH_2-$ signal (δ = 3.89 ppm) of PPP. The weight fraction of P3EHT in the synthesized PPP-*b*-P3EHT block copolymer was calculated as 59% according to the GPC results, leading to the measurement of M_n = 4.4k for the P3EHT block. Therefore, this PPP–P3EHT sample was denoted as **P30E44**.

Alternately, the co-crystalline structure of PPP and P3EHT is designated as P+E for shorthand. X-ray diffraction (XRD) (Fig. 3) and differential scanning calorimetry (DSC) (Fig. 4) measurements reveal the crystalline characteristic of the copolymers by preparing the bulk samples *via* slow drying from their THF solution (10 mg mL^{-1}), followed by heat-treatment above the melting temperature at 110 °C to remove the thermal history and annealing at a temperature of 40 °C (lower than the melting onset temperatures for both PPP (~50 °C) and P3EHT (~60 °C) homopolymers) for 1 day for equilibrium. The XRD diffraction patterns for homopolymers PPP and P3HHT are shown in Fig. S2† to compare with those of the diblock copolymers shown in Fig. 3.

Table 1 Summary of the molecular characteristics of PPP–P3EHTs

Samples	Designation	M_n PPP [g mol^{-1}]	M_n P3EHT [g mol^{-1}]	Φ_{P3EHT}	PDI
PPP-*b*-P3EHT	**P28E109**	2800	10 900	0.80	1.09
	P32E64	3300	6500	0.67	1.10
	P32E53	3300	5300	0.62	1.16
	P30E44	3100	4400	0.59	1.16
	P29E28	3000	2800	0.49	1.13
	P33E15	3300	1500	0.31	1.10
	P33E6	3400	640	0.16	1.17

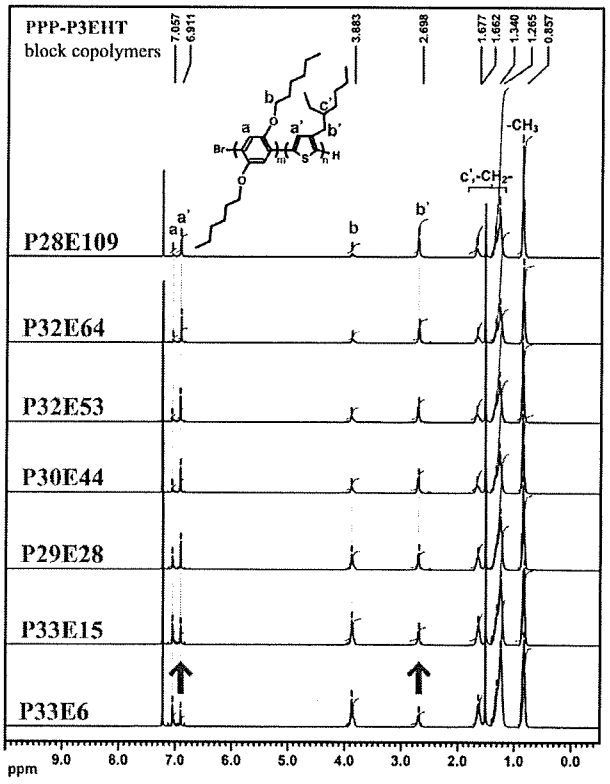

Fig. 2 ^{1}H NMR spectra of PPP–P3EHT block copolymers in $CDCl_3$.

Two sharp and intense peaks at 2θ = 2.8° and 2θ = 3.9° denoted as $(100)_P$ and $(100)_E$ (Fig. 3b) are the crystallographic (100) reflections corresponding to pristine PPP (P)[47] and P3EHT (E)[15] crystals, respectively. As shown in Fig. 3a, the scattering peaks associated with (100) reflections can be clearly observed for **P33E6** and **P28E109**, the two copolymers with the most extreme compositions. The (100) peak for **P33E6** and **P28E109** corresponds precisely to $(100)_P$ and $(100)_E$, respectively, indicating that they predominately form PPP and P3EHT crystals, respectively. In addition, no visible diffraction peaks for E and P minor phases were found for **P33E6** and **P28E109**, respectively. At low E fraction ($0.25 < \Phi_{P3EHT} < 0.50$) for **P33E15** and **P29E28**, these samples show a single but broader (100) diffraction peak, denoted as $(100)_{P+E}$ that shifts with increasing E fraction from 2θ = 3.0° to 2θ = 3.2°, indicating the shrinking of the corresponding *d*-spacing of the $(100)_{P+E}$ plane as detailed in Fig. 3b. Since the (100) plane for these π-conjugated homopolymers corresponds to their alkyl interchain distance between the main-chain backbones. The presence of a single diffraction peak with (100) domain spacing that is intermediate between those of the pristine PPP and P3EHT crystals indicates that PPP and P3EHT blocks are able to pack within a single P+E co-crystalline domain in which the hexyl side chains of PPP and the ethylhexyl side chains of P3EHT compromise to form a balanced (100) plane by adjusting their conformation. A similar co-crystalline structure with domain spacing intermediate between those of the two constituent P3AT-based homopolymers with different side chain structures has been found in the blend system.[48] In the blend system, the interlayer stacking of the two

Published on 29 January 2014. Downloaded by National Tsing Hua University on 07/07/2014 02:07:48.

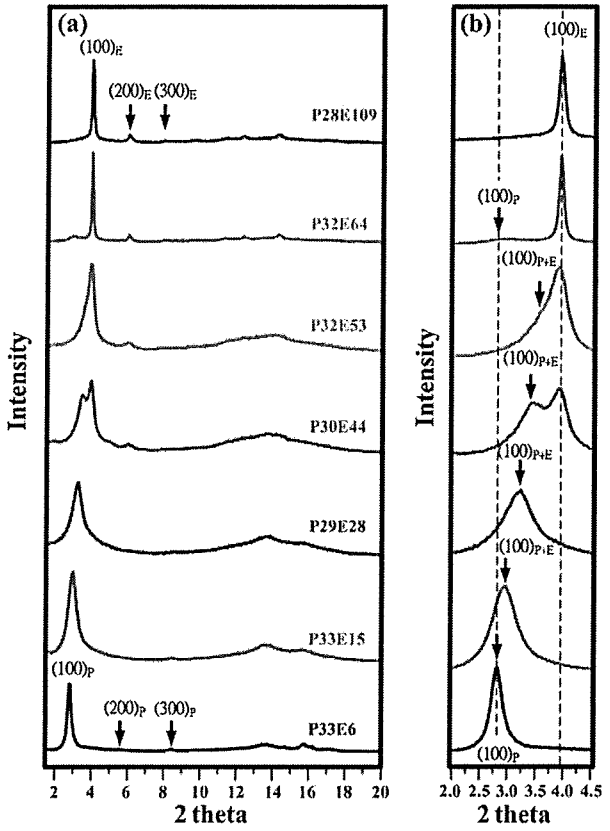

Fig. 3 XRD data of all PPP–P3EHTs that have been heat-treated above their melting temperature briefly and then annealed at 40 °C for 1 day. (a) The overall WAXS curves. (b) The WAXS curves for the (100) diffraction peak. The dashed-lines indicate the corresponding (100) plane for pristine PPP and P3EHT homopolymers.

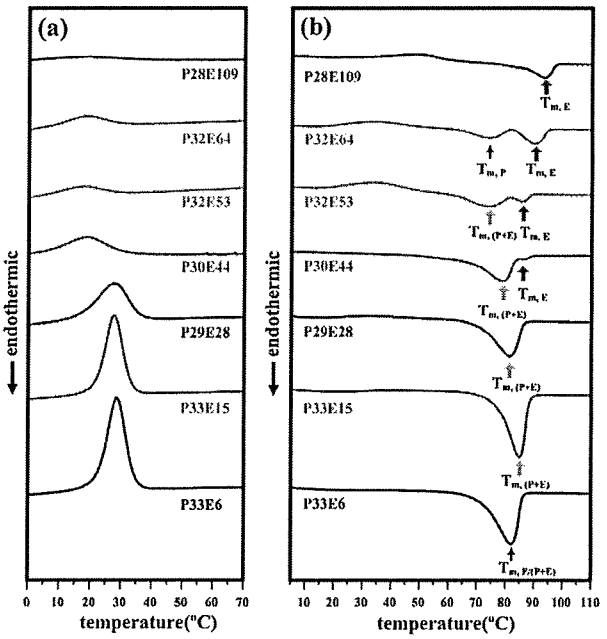

Fig. 4 DSC curves of all PPP–P3EHTs for (a) cooling scans at 10 °C min^{-1} and (b) second heating scans at 10 °C min^{-1}.

polymer main-chains can also be tuned by the composition of the two components in their cocrystals. In our current system, we also propose that PPP–P3EHT copolymers with dissimilar main-chains are capable of coexisting within the same crystalline domain with the interlayer stacking distance of the cocrystal (100) plane that is intermediate between those of the pristine PPP and P3EHT crystals. Note that there is a broadening of the (100) peak, indicating a decrease in the cocrystal size. Further DSC analysis shown in Fig. 4a confirms a single crystallization peak for both **P33E15** and **P29E28** with a single endothermic peak in the subsequently heating run (Fig. 4b). Therefore, WAXS and DSC results combine to show that both **P33E15** and **P29E28** form a single uniform co-crystalline structure with $(100)_{P+E}$ domain spacing that is close to an weight-average contribution from the individual pristine PPP and P3EHT crystals (Fig. S4†), indicating that the co-crystallite consists of PPP and P3EHT main-chains with mutually interdigitated side-chains spaced in-between.

The somewhat lower scattering intensity and broader full width at the half-maximum (FWHM) of the corresponding $(100)_{P+E}$ diffraction peak for **P29E28** (Fig. 3b) also indicates that the co-crystallite size in **P29E28** is smaller than that in **P33E15**, leading to a decrease in its melting points as shown in the DSC result (Fig. 4b). For the **P30E44** sample, a distinct feature has emerged in its WAXS spectrum which shows that there are not just one but two distinct diffraction peaks which correspond to the $(100)_{P+E}$ co-crystallites and $(100)_E$ P3EHT crystallites at $2\theta = 3.4°$ and $2\theta = 3.9°$, respectively. In the case of **P32E53**, the (100) peak can be roughly resolved into two distinct peaks (shown in Fig. S1†) at $2\theta = 3.5°$ and $2\theta = 3.9°$ due to the presence of both P+E co-crystallites and pure P3EHT crystallites. Accordingly, two endothermic peaks each corresponding to the P+E co-crystallite and P3EHT crystallite domains are also observed for **P30E44** and **P32E53** to confirm their presence. Notably, the existence of a simultaneous co-crystalline/crystalline domain structure is interesting since it may serve as a building block for self-organization of higher ordered superstructures (shown later from the SAXS measurements). To the best our knowledge, this is new experimental evidence to demonstrate the simultaneous presence of both co-crystallites and constituent crystallite for a block copolymer containing poly(3-alkylthiophene), forming a hierarchical co-crystalline/crystalline/self-assembled superstructure. It is worth noting that the d_{100}-spacing of the P+E co-crystalline domain decreases linearly with the increasing weight fraction of P3EHT shown in Fig. S4,† since more P3EHT blocks with smaller $d_{(100)}$-spacing were incorporated into the co-crystallite domain. Notably, a coexisting crystalline/crystalline structure was observed at an even higher P3EHT fraction for **P32E64** with separate $(100)_P$ and $(100)_E$ diffraction peaks since the self-crystallization of P3EHT may dominate the self-assembly behavior of the copolymer and thus may exclude the formation of P+E co-crystallites. Furthermore, the DSC measurement reveals that **P32E64** also exhibits two separate endothermic peaks with melting points at 75 °C and 90 °C as shown in Fig. 4b, confirming a microphase separated nanostructure with PPP and P3EHT crystallizing independently.

The apparently broad melting transition of **P33E6** compared to the sharp melting transition at 75 °C of a pure PPP

This journal is © The Royal Society of Chemistry 2014

Published on 29 January 2014. Downloaded by National Tsing Hua University on 07/07/2014 02:07:48.

homopolymer (result not shown) is likely because the prevailing PPP block partially co-crystallize with P3EHT for **P33E6**. In contrast, however, an amorphous PPP/crystalline P3EHT structure (Fig. 3) is observed at the highest P3EHT fraction for the **P28E109** sample, since the scattering peaks for crystalline PPP are not observed, confirming that the P3EHT block is the only crystalline component of the sample. The DSC heating thermograms shown in Fig. 4b also corroborate a single endothermic peak for **P28E109** around 90 °C which is close to the melting temperature of 91 °C of a pure P3EHT homopolymer. Therefore, by both DSC and WAXS results, we demonstrated the discovery of four categories of coexisting crystalline structures: PPP crystalline/P3EHT amorphous (schematically illustrated in Fig. 5a), P+E cocrystalline (Fig. 5b), P+E cocrystalline/P3EHT crystalline (Fig. 5c), and separate PPP crystalline/P3EHT crystalline (Fig. 5d) structures. Fig. 5a–d also exhibit higher order self-assembly nanostructures for each of the block copolymers which will be discussed in the following section.

In order to investigate the self-assembly behavior of the block copolymers on the nanoscale, small-angle X-ray scattering (SAXS) studies were also conducted. As shown in Fig. 6, a broad but distinct reflection peak at a scattering wave vector from 0.057 nm^{-1} to 0.06 nm^{-1} is observed for **P33E6**, **P30E15**, and **P29E28**, showing that the block copolymers can self-assemble into a higher order nanofibril crystalline structure with a domain spacing of ~10.4 nm to ~11.0 nm. The SAXS scattering profiles show that there are two broad peaks at q^* and $3q^*$ for **P30E44** and three distinct peaks at q^*, $2q^*$, and $3q^*$ for **P32E53**, suggesting there exists a microphase-separated lamellar structure consisting of a P+E cocrystalline domain for one of the bilayer lamellar structure and a P3EHT-rich crystalline domain for

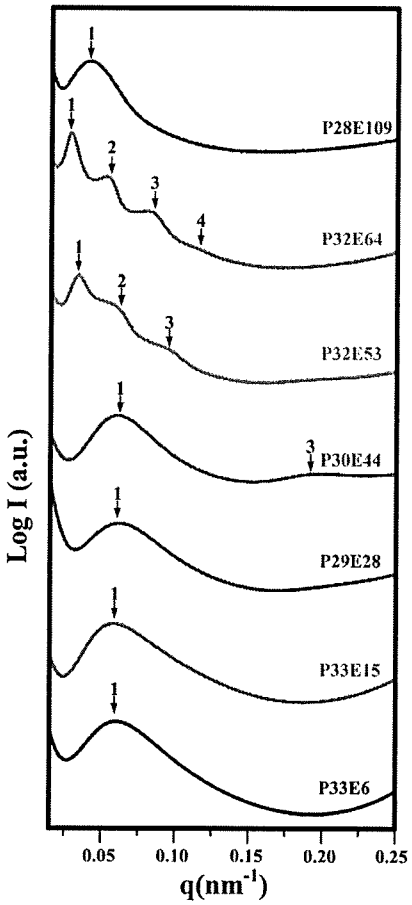

Fig. 6 SAXS curves for all PPP–P3EHT block copolymers with a fixed PPP M_n of ~3000 g per mole and varied P3EHT M_n (from 600 to 11 000 g per mole).

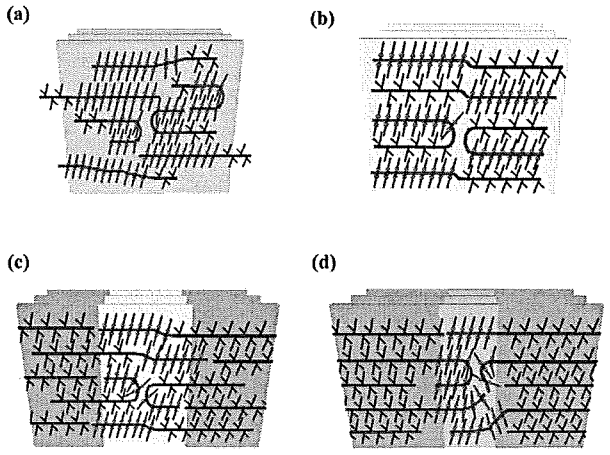

Fig. 5 Schematic depiction of the effect of relative block ratios on the crystalline structures in PPP–P3EHT all-conjugated BCPs. Blue and red chains are assigned for P3EHT and PPP segments, respectively. The purple, light blue, and yellow colors are assigned to the PPP-rich crystalline structure, P3EHT-rich crystalline structure, and PPP–P3EHT cocrystalline structure, respectively. These BCPs are able to self-assemble into different nanostructures of (a) crystalline–amorphous, (b) cocrystalline, (c) cocrystalline–crystalline, (d) crystalline–crystalline with increasing P3EHT ratios in the copolymer.

the other. Furthermore, we also observed a highly ordered lamellar structure for **P32E64**, based on the SAXS analysis of the ordered reflections observed at q^*, $2q^*$, $3q^*$, and $4q^*$, as demonstrated in Fig. 6. The well-ordered lamellar structure thus formed because the P+E co-crystallite can no longer form at this high P3EHT fraction, resulting from the self-crystallization characteristics of each block, as evidenced by the above-mentioned WAXS and DSC analyses. We observed, however, only one reflection peak (Fig. 6) at the highest P3EHT fraction for **P28E109**, which is likely due to the large difference in the molecular weight between PPP and P3EHT, leading to the formation of a domain with crystalline P3EHT nanofibrils and much less organized amorphous packing of PPP segments. Combined together with the previously WAXS results, we obtained a PPP amorphous/P3EHT crystalline structure for **P28E109** and it exhibits a self-assemble nanofibrillar morphology, which will be further confirmed by the subsequent TEM analysis (Fig. 7) and AFM measurement (Fig. 8).

To investigate the self-assembly morphology of PPP–P3EHT, their microphase-separated hierarchical superstructures are characterized by transmission electron microscopy (TEM). All copolymers were microtomed with a thickness of <100 nm and

Published on 29 January 2014. Downloaded by National Tsing Hua University on 07/07/2014 02:07:48.

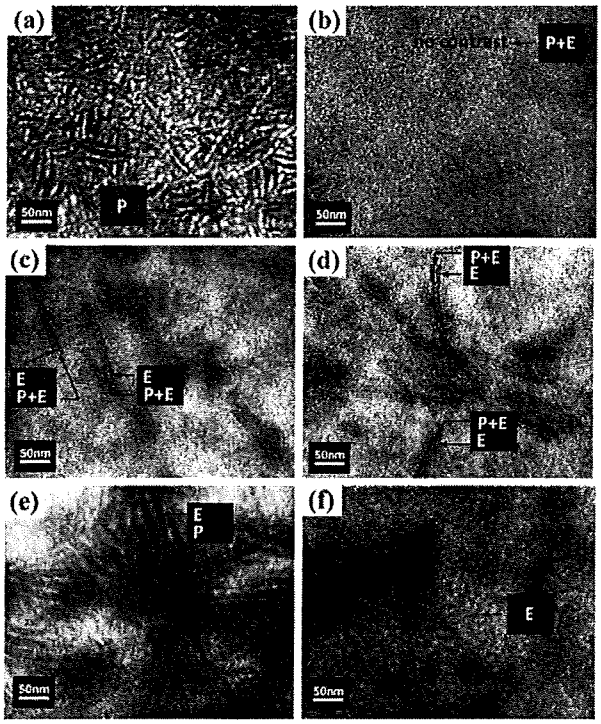

Fig. 7 TEM images of stained microstructures of (a) P nanofibrils for P33E6, (b) fully P + E cocrystalline nanofibrils for P29E28, (c and d) a cocrystalline–crystalline lamellar structure composed of a P + E cocrystalline layer and an E crystalline domain for P30E44 and P32E53, (e) a lamellar structure consisting of P and E layers for P32E64, and (f) E nanofibril morphology for P28E109.

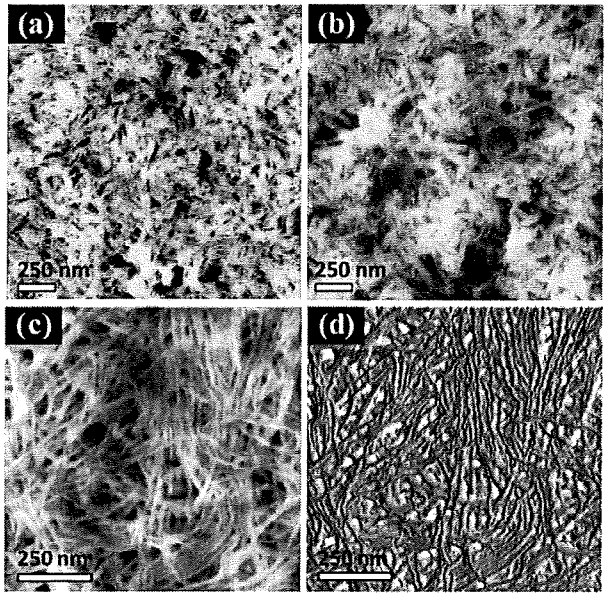

Fig. 8 Atomic force microscopy (AFM) height images of thin films of (a) P33E15, (b) P29E28 and (c) P28E109. (d) AFM phase image of a thin film of P28E109. All three samples display characteristic nanofibril morphology.

subsequently stained with RuO_4 vapors for 5 min to show a dark region for the P3EHT domain under TEM. The TEM image of the **P33E6** (Fig. 7a) indicated that there exists a nanofibril bulk microstructure with a fibrillar width estimated at ~10 nm, which is consistent with the SAXS results. As P3EHT fraction increases further, there are no stark-contrast structures observed in the corresponding TEM images for **P33E15** and **P29E28** (Fig. 7b) due to the co-crystallization nature of an interchain structure with PPP and P3EHT main-chains packed within as sketched in Fig. 5b since staining can only be achieved with the presence of a large P3EHT domain.

The co-crystallization structure of **P33E15** and **P29E28** without TEM contrast can be revealed by the characterization of atomic force microscope (AFM) measurement of their thin spin-coated films. As shown in Fig. 8, its height images show clear nanopatterns with the fibril microstructures for both **P33E15** and **P29E28**, which are consistent with the SAXS and DSC data shown above. Note that the self-assembled structures of **P30E44** and **P32E53** are determined by the microphase separation lamella structure with a P+E co-crystallized layer and a P3EHT crystallized layer. The width of the P3EHT layer is roughly 4–5 nm (stained dark selectively with RuO_4) estimated from the TEM measurement, which is significantly smaller than the theoretical fully extended chain length for P3EHT. The result indicates that for **P30E44** and **P32E53**, a significant amount of P3EHT block has been incorporated into the co-crystalline domain layer and the remaining short P3EHT chains, therefore, form a separate and narrower layer with a domain spacing of only 4–5 nm in the lamellar structure.[40] In addition, to the best of our knowledge, the images shown in Fig. 7c and d are the first cocrystalline lamella images taken using TEM for all-conjugated block copolymers. In contrast, a bilayer crystalline/crystalline lamellar structure (Fig. 7e) is observed for **P32E64**, which has a characteristic P3EHT domain of around 11–12 nm, and it is significantly different from the P3EHT domain for **P30E44** and **P32E53** (4–5 nm), also indicating that a significant amount of P3EHT is incorporated into these two block copolymers as a co-crystalline domain. Since **P32E64** exhibits no co-crystalline structure, **P32E53** presents the highest composition in the series above which the co-crystalline domain can no longer be obtained. Lastly, predominately P3EHT nanofibrillar morphology was observed for **P28E109** with the highest P3EHT fraction shown in Fig. 7f. Additionally, the morphology of **P28E109** can be further measured by using AFM. In Fig. 8(c) and (d), the height and phase images, respectively, of a nanofibrillar structure for **P28E109** can be observed.

The self-assembly behavior of PPP–P3EHT block copolymers reveals two important parameters including the self-crystallization and co-crystallization of the dissimilar polymers that dictate their molecular packing. Note that no co-crystal structure was observed for **P28E109**, yet a co-crystalline P+E domain appears in **P33E6**, which is likely due to the large difference in the crystallization enthalpy between PPP and P3EHT blocks (Fig. 4a). The formation of the P+E co-crystals was driven by a large crystallization enthalpy of PPP that allows incorporation of less crystallizable P3EHT into the domain for **P33E6**. Thus, for PPP-rich samples (**P33E6**, **P33E15**, and **P29E28**), the co-

This journal is © The Royal Society of Chemistry 2014

Published on 29 January 2014. Downloaded by National Tsing Hua University on 07/07/2014 02:07:48.

crystallization effect acts as the primary driving force in molecular packing, and therefore the co-crystalline P+E domain dominates the self-assembly behavior of block copolymers. Upon increasing the P3EHT fraction (**P30E44** and **P32E53**), the P3EHT segment is long enough to form its own crystalline domain, and subsequently the competition balance of self-crystallization and co-crystallization effects that favors the formation of separated co-crystalline P+E and P3EHT domains leads to a bilayer co-crystalline/pure crystalline P3EHT lamellar structure instead of only co-crystalline P+E molecular packing. With further increasing P3EHT fraction (**P32E64**), the much longer P3EHT block exhibits profound self-crystallization ability and suppress the co-crystallization formation of PPP and P3EHT. Thus, the self-assembly behavior of the copolymers is mainly driven by the self-crystallization of the dissimilar blocks, resulting in a microphase-separated bilayer PPP–P3EHT lamellar structure. However, for **P28E109**, the crystallization enthalpy for P3EHT is relatively small such that PPP cannot be energetically incorporated into a single cocrystal domain, therefore, only P3EHT crystals were observed.

To summarize, we demonstrate that a series of PPP–P3EHT cocrystallizable block copolymers which can be self-assembled into four different superstructures, enabling PPP–P3EHT to be a suitable model for exploring the cocrystallization nature and the nanoscale pattern of the rod–rod all-π-conjugated BCPs.

4. Conclusions

In summary, we have synthesized a series of all-conjugated crystalline–crystalline block copolymers and the superstructures were also observed in a competing balance between self-crystallization of an individual block and co-crystallization from dissimilar blocks by a combination of WAXS, DSC, SAXS, TEM, and AFM measurements. This is the first experimental study for the presence of the co-crystallization structure of all-conjugated BCPs with different main-chain components. Our results suggest that all-π-conjugated BCPs with different main-chain moieties are an excellent system for further exploring the co-crystallization nature and self-assembly behavior of all-conjugated block copolymers.

Acknowledgements

The financial support from the National Science Council of Taiwan is greatly appreciated. The X-ray measurements were conducted at the National Synchrotron Radiation Research Center (NSRRC) in Taiwan. The authors would also like to thank Dr U-Ser Jeng and Dr Ming-Tao Lee for their help during the X-ray experiments at NSRRC.

References

1 D. Guenes, H. Neugebauer and N. S. Sariciftci, *Chem. Rev.*, 2007, **107**, 1324–1338.
2 P. W. M. Blom, V. D. Mihailetchi, L. J. D. Koster and D. E. Markov, *Adv. Mater.*, 2007, **19**, 1551–1566.
3 A. P. Kulkarni, C. J. Tonzola, A. Babel and S. A. Jenekhe, *Chem. Mater.*, 2004, **16**, 4556–4573.
4 C. D. Dimitrakopoulos and P. R. L. Malenfant, *Adv. Mater.*, 2002, **14**, 99–117.
5 V. Coropceanu, J. Cornil, D. A. da Silva Filho, Y. Olivier, R. Silbey and J.-L. Bredas, *Chem. Rev.*, 2007, **107**, 926–952.
6 J. A. Osaheni and S. A. Jenekhe, *J. Am. Chem. Soc.*, 1995, **117**, 7389–7398.
7 C. L. Donley, J. Zaumseil, J. W. Andreasen, M. M. Nielsen, H. Sirringhaus, R. H. Friend and J. S. Kim, *J. Am. Chem. Soc.*, 2005, **127**, 12890–12899.
8 V. Ho, B. W. Boudouris and R. A. Segalman, *Macromolecules*, 2010, **43**, 7895–7899.
9 X. N. Yang, J. Loos, S. C. Veenstra, W. J. H. Verhees, M. M. Wienk, J. M. Kroon, M. A. J. Michels and R. A. J. Janssen, *Nano Lett.*, 2005, **5**, 579–583.
10 Y. Tao, B. McCulloch, S. Kim and R. A. Segalman, *Soft Matter*, 2009, **5**, 4219–4230.
11 C.-A. Dai, W.-C. Yen, Y.-H. Lee, C.-C. Ho and W.-F. Su, *J. Am. Chem. Soc.*, 2007, **129**, 11036–11038.
12 I. Botiz and S. B. Darling, *Macromolecules*, 2009, **42**, 8211–8217.
13 I. Botiz, A. B. F. Martinson and S. B. Darling, *Langmuir*, 2010, **26**, 8756–8761.
14 Y.-H. Lee, C.-J. Chang, C.-J. Kao and C.-A. Dai, *Langmuir*, 2010, **26**, 4196–4206.
15 V. Ho, B. W. Boudouris, B. L. McCulloch, C. G. Shuttle, M. Burkhardt, M. L. Chabinyc and R. A. Segalman, *J. Am. Chem. Soc.*, 2011, **133**, 9270–9273.
16 Y.-H. Lee, W.-C. Yen, W.-F. Su and C.-A. Dai, *Soft Matter*, 2011, **7**, 10429–10442.
17 C.-J. Chang, Y.-H. Lee, H.-L. Chen, C.-H. Chiang, H.-F. Hsu, C.-C. Ho, W.-F. Su and C.-A. Dai, *Soft Matter*, 2011, **7**, 10951–10960.
18 S. N. Patel, A. E. Javier, K. M. Beers, J. A. Pople, V. Ho, R. A. Segalman and N. P. Balsara, *Nano Lett.*, 2012, **12**, 4901–4906.
19 C.-S. Lai, C.-C. Ho, H.-L. Chen and W.-F. Su, *Macromolecules*, 2013, **46**, 2249–2257.
20 S. B. Darling, *Energy Environ. Sci.*, 2009, **2**, 1266–1273.
21 I. Botiz and S. B. Darling, *Mater. Today*, 2010, **13**, 42–51.
22 Y. Zhang, K. Tajima, K. Hirota and K. Hashimoto, *J. Am. Chem. Soc.*, 2008, **130**, 7812–7813.
23 R. Miyakoshi, A. Yokoyama and T. Yokozawa, *Chem. Lett.*, 2008, **37**, 1022–1023.
24 K. Ohshimizu and M. Ueda, *Macromolecules*, 2008, **41**, 5289–5294.
25 Y. Zhang, K. Tajima and K. Hashimoto, *Macromolecules*, 2009, **42**, 7008–7015.
26 P.-T. Wu, G. Ren, C. Li, R. Mezzenga and S. A. Jenekhe, *Macromolecules*, 2009, **42**, 2317–2320.
27 S. Wu, L. Bu, L. Huang, X. Yu, Y. Han, Y. Geng and F. Wang, *Polymer*, 2009, **50**, 6245–6251.
28 U. Scherf, S. Adamczyk, A. Gutacker and N. Koenen, *Macromol. Rapid Commun.*, 2009, **30**, 1059–1065.
29 R. Verduzco, I. Botiz, D. L. Pickel, S. M. Kilbey, K. L. Hong, E. Dimasi and S. B. Darling, *Macromolecules*, 2011, **44**, 530–539.

Published on 29 January 2014. Downloaded by National Tsing Hua University on 07/07/2014 02:07:48.

30 I. Botiz, R. D. Schaller, R. Verduzco and S. B. Darling, *J. Phys. Chem. C*, 2011, **115**, 9260–9266.
31 Y. H. Lin, S. B. Darling, M. P. Nikiforov, J. Strzalka and R. Verduzco, *Macromolecules*, 2012, **45**, 6571–6579.
32 K. A. Smith, Y. H. Lin, D. B. Dement, J. Strzalka, S. B. Darling, D. L. Pickel and R. Verduzco, *Macromolecules*, 2013, **46**, 2636–2645.
33 M. He, L. Zhao, J. Wang, W. Han, Y. Yang, F. Qiu and Z. Lin, *ACS Nano*, 2010, **4**, 3241–3247.
34 J. Kim, I. Y. Song and T. Park, *Chem. Commun.*, 2011, **47**, 4697–4699.
35 E. Lee, B. Hammer, J.-K. Kim, Z. Page, T. Emrick and R. C. Hayward, *J. Am. Chem. Soc.*, 2011, **133**, 10390–10393.
36 J. Hollinger, P. M. DiCarmine, D. Karl and D. C. Seferos, *Macromolecules*, 2012, **45**, 3772–3778.
37 Y.-H. Lin, K. A. Smith, C. N. Kempf and R. Verduzco, *Polym. Chem.*, 2013, **4**, 229–232.
38 X. Zhang, W. Yang, F. Kong, H. Yang and B. Lin, *Polym. Int.*, 2013, **62**, 204–209.
39 J. Ge, M. He, F. Qiu and Y. Yang, *Macromolecules*, 2010, **43**, 6422–6428.
40 C.-C. Ho, Y.-C. Liu, S.-H. Lin and W.-F. Su, *Macromolecules*, 2012, **45**, 813–820.
41 R. Miyakoshi, K. Shimono, A. Yokoyama and T. Yokozawa, *J. Am. Chem. Soc.*, 2006, **128**, 16012–16013.
42 R. S. Lowe, S. M. Khersonsky and R. D. McCullough, *Adv. Mater.*, 1999, **11**, 250–253.
43 R. S. Lowe, P. C. Ewbank, J. Liu, L. Zhai and R. D. McCullough, *Macromolecules*, 2001, **34**, 4324–4333.
44 R. Miyakoshi, A. Yokoyama and T. Yokozawa, *J. Am. Chem. Soc.*, 2005, **127**, 17542–17547.
45 E. L. Lanni, J. R. Locke, C. M. Gleave and A. J. McNeil, *Macromolecules*, 2011, **44**, 5136–5145.
46 Z. J. Bryan, M. L. Smith and A. J. McNeil, *Macromol. Rapid Commun.*, 2012, **33**, 842–847.
47 X. Yu, H. Yang, S. Wu, Y. Geng and Y. Han, *Macromolecules*, 2012, **45**, 266–274.
48 Y. Qu, L. Li, G. Lu, X. Zhou, Q. Su, W. Xu, S. Li, J. Zhang and X. Yang, *Polym. Chem.*, 2012, **3**, 3301–3307.

This journal is © The Royal Society of Chemistry 2014